# The Scaling and Structure of the Estuarine Bottom Boundary Layer

MARK T. STACEY AND DAVID K. RALSTON

*Department of Civil and Environmental Engineering, University of California, Berkeley, Berkeley, California*

(Manuscript received 18 September 2003, in final form 6 July 2004)

ABSTRACT

A two-week dataset from a partially and periodically stratified estuary quantifies variability in the turbulence across the tidal and spring–neap time scales. These observations have been fit with a two-parameter model of the Reynolds stress profile, which produces estimates of the time variation of the bottom boundary layer height and the friction velocity. Conditions at the top of the bottom boundary layer indicate that the dynamics governing the development of the estuarine bottom boundary layer are different on ebb tides than on flood tides. The asymmetry in the flow is explained by consideration of the strain-induced buoyancy flux, which is stabilizing on ebb tides and destabilizing on flood tides. Based on these observations, a scaling approach to estimating estuarine bottom boundary layer parameters (height and friction velocity) is presented, which includes a modified Monin–Obukhov length scale to account for the horizontal buoyancy flux created by the sheared advection. Comparison with the observations of boundary layer height and friction velocity suggests that this approach may be successful in predicting bottom boundary layer parameters in estuaries and coastal regions with significant horizontal buoyancy fluxes. Comparison between the strain-induced buoyancy flux and shear production indicates that the straining of the density field is an important contributor to the turbulent kinetic energy budget and creates an asymmetry in turbulent energy between ebb and flood tides. It appears that the structure of the turbulence, specifically the ratio of the Reynolds stress to the turbulent energy, is also modified by tidal straining, further accentuating the ebb–flood asymmetries.

## 1. Introduction

The description and prediction of turbulent mixing in a stratified tidal flow are fundamental to our ability to effectively determine transport and mixing in coastal and estuarine environments. At the same time, the presence of density gradients, in both vertical and horizontal directions, modifies the distribution, magnitude, and timing of mixing. On its own, the interaction of turbulence, stratification, and shear poses a challenge to turbulence modeling (see, e.g., Itsweire et al. 1993; Burchard et al. 1998). The presence of horizontal density gradients further confound this analysis through the straining of the background density field by sheared horizontal flows. To be specific, the interaction of the tidal velocities and the horizontal (longitudinal in estuaries) density gradient creates strain-induced periodic stratification (SIPS; Simpson et al. 1990). Periodic stratification occurs when the water column destratifies regularly in the tidal cycle; if the stratification persists, the estuary would be considered partially or strongly stratified, depending on the relative strength of the tides (see, e.g., Jay and Smith 1990a,b). Even in a partially or strongly stratified system, the straining of the density field by tidal flows results in a dynamic density structure, with tidal time-scale variability in the level of stratification. Finally, the direction of the buoyancy gradient along the axis of the estuary creates an asymmetry that may manifest itself as significant ebb–flood asymmetries in the structure of the tidal currents (Cudaback and Jay 2000) and in turbulent mixing (Rippeth et al. 2001; Stacey et al. 1999a; Geyer et al. 2000).

In strongly stratified and sheared systems, production of turbulence is primarily in the interior of the flow, through shear instabilities or the breaking of internal waves (Jay and Smith 1990a). In partially or periodically stratified estuaries, however, shear production near the bed will be dominant, and a well-mixed bottom boundary layer would be expected to develop (e.g., Lu et al. 2000). While a scaling approach to boundary layer development has been applied successfully to the coastal ocean (see, e.g., Trowbridge and Lentz 1991), the estuarine boundary layer, and the constraints imposed by density stratification, have received less attention.

The lack of activity in estuaries is largely attributable to gaps in observations of estuarine turbulence. Re-

*Corresponding author address:* Dr. Mark T. Stacey, University of California, Berkeley, Environmental Fluid Mechanics, 631 Davis Hall #1710, Berkeley, CA 94720-1710.
E-mail: mstacey@socrates.berkeley.edu

cently, however, the details of turbulence and turbulent mixing in estuaries have been more thoroughly examined, with new technologies being employed for detecting both large-scale turbulent parameters (Lu and Lueck 1999; Stacey et al. 1999a,b; Rippeth et al. 2001) and small-scale turbulent shears (Gregg 1987; Peters and Bokhorst 2000, 2001). These observations have all suggested that estuarine turbulence is highly variable at the tidal and spring–neap time scales, most likely due to the complex interaction between density stratification and shear production. In most cases, shallow estuarine systems are characterized by a well-mixed bottom boundary layer, capped overhead by a stable density gradient. The competition between shear production within the bottom boundary layer (BBL) and the density dynamics at the top of the boundary layer define the extent and energetics of mixing within the BBL.

In this paper, we will describe the evolution and structure of the estuarine bottom boundary layer over a spring–neap cycle. The datasets are described in the next two sections. Following this introduction to the data and conditions we will estimate the boundary layer parameters and develop a scaling argument to predict their variability. Last, we will examine the details of the turbulence within the bottom boundary layer, including its kinetic energy and the relation between energy and momentum transfer.

## 2. Experiment description

In October 1999, a comprehensive study of the dynamics of an estuarine channel was performed in Suisun Cutoff in northern San Francisco Bay (Fig. 1). The study site was chosen to minimize the effects of lateral variations and Suisun Cutoff provides a straight, narrow channel of a relatively uniform depth of 10 m with minimal shoal areas. Previous studies (Stacey et al. 1999a) indicated that turbulence at the site was quite variable on the tidal time scale with periodic stratification developing during neap tides. The goal of the current experiment was to examine the variation in mixing on the spring–neap time scale and to allow a consideration of the subtidal dynamics. With this in mind, measurements were made over a two-week period extending from 15 to 28 October 1999.

Before discussing the details of the data collected at the site, we present an overview of the conditions during the study period. These data were collected with the instrumentation described below and the details of the data collection can be found there. During the study period, the depth-averaged tidal currents went through an entire neap–spring cycle (Fig. 2a). In San Francisco Bay, the neaps are characterized by a strong diurnal inequality (days 288–293), while the spring tides are more symmetric (days 296–300). The depth-averaged

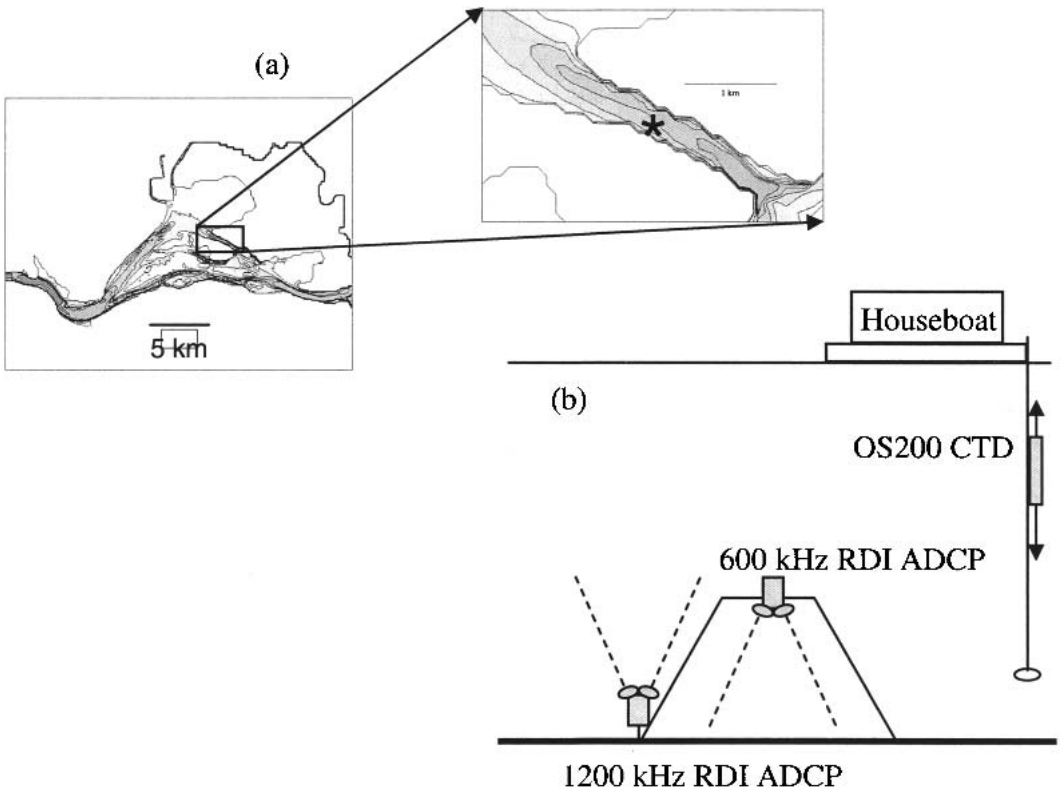


FIG. 1. Experiment setup: (a) location map and (b) instrument deployment. Location of deployment is marked by the asterisk in (a).

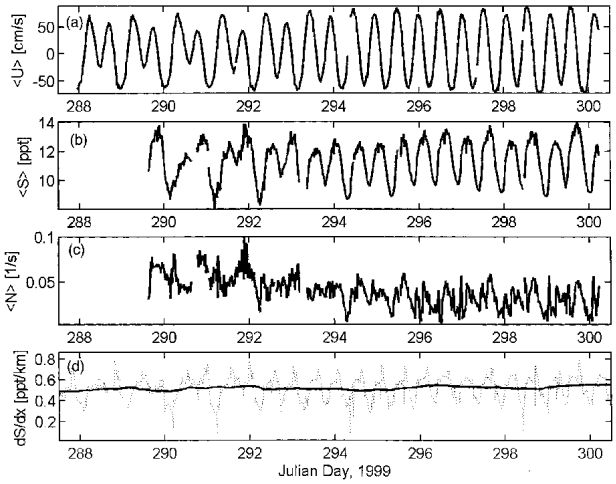


FIG. 2. Overview of conditions during experiment: (a) depth-averaged velocity, (b) depth-averaged salinity, (c) depth-averaged buoyancy frequency, and (d) depth-averaged longitudinal salinity gradient.

salinity (Fig. 2b) illustrates the dynamic nature of the flows at the site, with tidal time-scale variations in depth-averaged salinity of as much as 5 ppt during the neaps. The range of variability in the salinity is reduced during the springs due to a reduction in the diurnal inequality (Fig. 2c). As the tides transition from neaps to springs, the depth-averaged stratification is reduced by approximately a factor of 4 between days 290–292 (neaps) and days 298–300 (springs). We expect, therefore, to see a transition in the distribution and magnitude of mixing as the tides transition from neaps to springs. Last, buoyancy forcing, as measured by the depth-averaged longitudinal salinity gradient (Fig. 2d), is relatively constant throughout the study, at least in a tidally averaged sense. The tidal variations in this quantity are likely due to small-scale frontal features, and the tidally averaged gradient is most representative of the bulk buoyancy forcing.

The data to be discussed in this paper were collected from a bottom-mounted pair of broadband acoustic Doppler current profilers (BB-ADCPs, RD Instruments; 1200-kHz upward-looking, 600-kHz downward-looking) deployed in an up–down frame (Fig. 1c). The downward-looking BB-ADCP collected data in a high-resolution mode to capture the details of the near-bed velocity structure. Initial analysis of that data suggests that the high-resolution mode in the BB-ADCP may not be well suited for the measurement of turbulence because of a velocity-dependent decorrelation error. The upward-looking ADCP was mounted with its transducers 50 cm above the bed and had its first depth cell centered at 1.25 m above the bed. The instrument was configured to collect single-ping data in mode 1 with 25-cm bins, resulting in a data rate of slightly over 1 Hz. All data were communicated via cable to a houseboat anchored nearby and logged continuously on a computer. Deployed from the houseboat was a CTD profiler (OceanSensors), which was lowered from the houseboat through the water column every 15 min from an autonomous winch. The analysis of these datasets will be described in the next section.

Additional data collection at the site consisted of mean velocity profiles at four sites, continuous density profiles at either end of the channel, lateral velocity and density transects performed on 3 days throughout the two-week period, near-bed acoustic Doppler velocimeter (ADV), and velocity microstructure measurements. The lateral structure of the flow is discussed by Lacy et al. (2003) and has been found to have an important effect on the stratification of the water column late in the flood tides. Taken together, these measurements provide a comprehensive dataset to examine the overall dynamics of a stratified estuarine channel. In this paper, we will focus on the structure of the estuarine boundary layer and how it varies through the tidal and spring–neap cycles. In view of this emphasis, our analysis will focus on the upward-looking ADCP (which covered the entire water column) and the adjacent CTD profiler. In the next section, we provide an overview of that data.

## 3. Overview of data

The temporal resolution of all the data collected provided us with some flexibility in the choice of ensemble period. Previous studies at the site demonstrated that the flow is statistically stationary on a time scale of 15–20 min (Stacey 1996). Based on these results, we chose to work with a 10-min temporal resolution for all of the datasets. The ADCP data had a vertical resolution of 25 cm, which was the grid used for the other datasets as well.

The single-ping velocity data were block-averaged every 10 min to define the mean velocity (depth-averaged velocity shown in Fig. 2a). The data have been rotated into along-channel and cross-channel components based on the local geometry, and the flow is strongly channelized along the axis of Suisun Cutoff. Although the subtle lateral currents can be important during certain phases of the tide (Lacy et al. 2003), the along-channel shear production is considerably larger than the lateral shear production, and we will assume in this paper that the energetics of mixing are dominated by the along-channel component.

The density data from the OS200 profiler were averaged vertically in blocks of 10 samples, producing a vertical resolution of approximately 10 cm, but with some variability due to variation in the rate of profiling. Because the range of profiling was fixed and the winch was mounted on a floating platform, there was a data gap in the near-bed region that would vary with the tides, being largest at high tide and smallest at low tides (range 0.5–1.5 m). The first step in the analysis of the

density data, therefore, was to project these data onto a uniform vertical grid so that they could be analyzed in conjunction with the ADCP data collected at the site.

To extrapolate these profiles into the near-bed region, we applied the approach used to extrapolate velocity data to a free surface (Geyer et al. 2000). The bottom boundary condition for density (or, more specifically, salinity and temperature) is no flux, just as the surface boundary condition for velocity is no stress. As a result, the vertical density gradient must be zero at the bottom boundary. In order to extrapolate the measured density data to the bed, we linearly interpolated the density gradient from its last measured value (based on the lowest three density measurements) to zero at the bed. Frequently, the measured profile extended into the bottom mixed layer, and this extrapolation was essentially constant. More generally, however, the extended density profile in the bottom layer was quadratic, the same as results for the extrapolation of the velocity profile in the surface layer.

Once this extrapolation to the bed was defined, a spline interpolation (DeBoor 1978) was applied to the entire profile (including the extrapolated portion near the bed) to define the vertical density structure on the same 25-cm grid as the ADCP data. Last, the density profiles were linearly interpolated in time onto the same 10-min resolution used for the calculation of the mean velocity and turbulence quantities. The resulting dataset (Fig. 3a) shows a density field that is considerably more variable during the neaps (days 290–292) than during the springs (days 298–300), both in terms of the temporal variation with the tides and the stratification evident in the vertical structure. The stratification, defined as

$$N^2 = -\frac{g}{\rho_0}\frac{\partial \rho}{\partial z}$$

(where $g$ is the gravitational acceleration, $\rho$ is the density, and $\rho_0$ is a constant background density) and shown in Fig. 3b, is moderate during the neap period ($N^2 \approx 10^{-3}$ s$^{-2}$), but the water column becomes fairly well mixed during the springs, particularly during the flood tides ($N^2$ as low as $10^{-5}$–$10^{-6}$ s$^{-2}$, and even negative at times). Spatially, the portion of the water column that destratifies is limited to a small near-bed region during the neaps but grows to include much of the water column during the springs.

The single-ping velocity data were analyzed following the variance method outlined by Stacey et al. (1999b) and applied to observations from an energetic tidal channel by Rippeth et al. (2002). The analysis defines the ensemble-averaged Reynolds stresses and an estimate of the turbulent kinetic energy. Each 10-min ensemble consisted of over 600 pings (range from 607 to 612), resulting in errors in the Reynolds stress and TKE of approximately 2.3 cm$^2$ s$^{-2}$. Using a histogram of the minimum of TKE (see Stacey et al. 1999b for more details), the bias in TKE was determined to be 38 cm$^2$ s$^{-2}$, implying a per-ping velocity error of 6.2 cm s$^{-1}$,

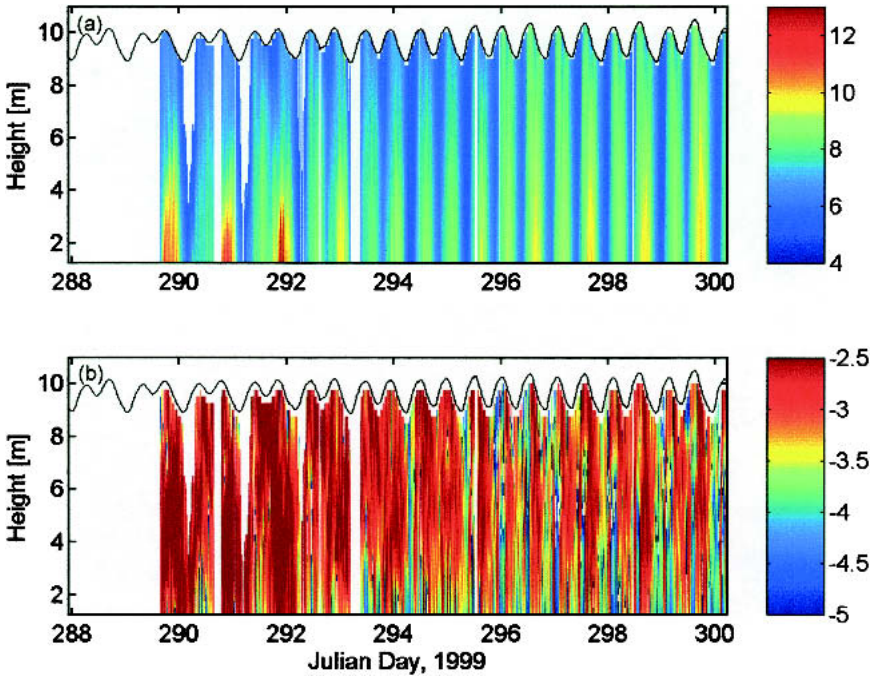


FIG. 3. Density structure based on CTD profiles: (a) density in $\sigma_t$ units and (b) $\log_{10}$ of buoyancy frequency squared (s$^{-2}$). Autonomous profiler did not begin deployment until late in day 289; other gaps are due to profiler malfunction.

which is slightly better than the RD Instruments reported error of 8.5 cm $s^{-1}$.

The resulting data quantify turbulent mixing throughout the water column over a neap–spring tidal cycle. Although the details of the neap–spring transition are beyond the scope of this paper, we present here the full data (Fig. 4) to set the stage for the discussion of the estuarine BBL in the remainder of the paper. The primary feature of the Reynolds stress (Fig. 4a) and the turbulent kinetic energy (Fig. 4b) is the bottom boundary layer, which has a clear tidal modulation both in terms of its extent through the water column and the magnitude of the turbulence properties. In both the stresses and the energy, however, there is a distinct transition from the neap tides to the spring tides, which is related to the transition from large diurnal inequalities and ebb–flood asymmetries (during the neaps) to symmetric tides during the springs.

## 4. Observations of estuarine BBL

The general water column structure of the turbulence is seen to consist of an energetic bottom boundary layer, the height of which is set by the interaction of the turbulence with the overlying stratification. Under an assumption of an unstratified, or weakly stratified bottom boundary layer, we would expect the magnitude of the Reynolds stresses to decrease nearly linearly upward from the bed, approaching zero at the top of the BBL. To fit this model to our data, we have two tunable parameters: the friction velocity squared, $u_*^2$, and the height of the bottom boundary layer, $h_{\mathrm{BBL}}$ (Fig. 5). The resulting model for the Reynolds stress in the BBL is

$$\overline{u'w'}_m(z) = u_*^2\left(1 - \frac{z}{h_{\mathrm{BBL}}}\right), \tag{1}$$

where $z$ is the height above the bed and $\overline{u'w'}_m$ indicates our model of the Reynolds stress profile. It should be noted that, if stratification modifies the boundary layer structure, a third parameter (a quadratic coefficient) would also be included in this formulation. The quality of fit with the quadratic model, however, was not significantly superior to the two parameter approach discussed here and the unstratified formulation will be applied.

Fitting this function to each profile of the Reynolds stresses results in time series of the two boundary layer parameters, $u_*^2$ and $h_{\mathrm{BBL}}$. Tests of the consistency of the model with the data need to be considered carefully in this case due to the fact that typical measures of statistical consistency [e.g., correlation coefficient squared ($R^2$)] would be indeterminant for the region outside the boundary layer (where the model is set to zero). As a result, we have applied a hybrid test of model–data consistency in which we require that the model has an $R^2$ value greater than 0.5 within the boundary layer

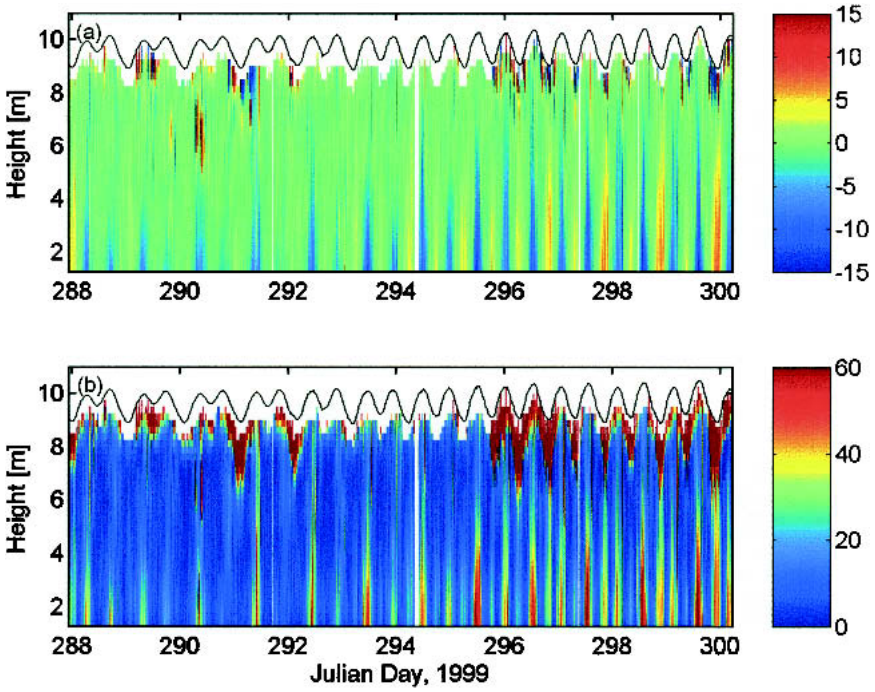


FIG. 4. Turbulence variability across entire dataset: (a) along-channel Reynolds stress ($cm^2\ s^{-2}$) and (b) turbulent kinetic energy ($cm^2\ s^{-2}$). High values of TKE near surface are actually manifestation of wind-wave orbital motions. Gaps (white bands) are due to stops in data collection for data download and backup.

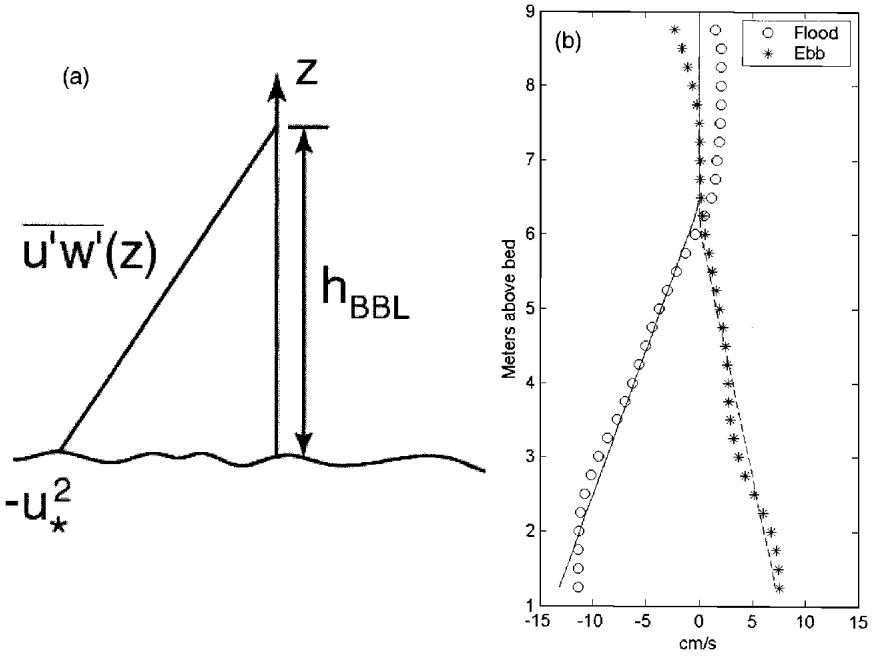


FIG. 5. Sketch of (a) function [Eq. (1)] used to fit Reynolds stresses and (b) sample profiles from the spring tide period. Lines in (b) show functional fit to data.

and, further, that the profile as a whole (including the region above the boundary layer) be positively correlated with the data. This eliminates those profiles where large midcolumn stresses occur, which result in a negative correlation for the whole profile.

In Fig. 6, the results of this fitting are displayed for those fits that meet the above criteria, but with a 1-h block-average of $h_{\mathrm{BBL}}$. The height of the BBL (Fig. 6b) is variable on the tidal time scale, deepening during each flood or ebb tide and shrinking during the intervening slack tides. At a longer time scale, a slight increase in the depth of the BBL is also evident during spring tides as opposed to the neaps.

The friction velocity (Fig. 6c) clearly varies on the tidal time scale, with flood tides characterized by negative values and ebb tides by positive values, as is expected physically. In this data, the transition from neaps to springs is profound—during the neap tide, the friction velocity on ebbs is nearly zero but becomes more symmetric between floods and ebbs during the spring tide.

In general, the structure of the BBL is characterized by an asymmetry between ebb and flood tides. During the neaps, the ebb tide BBL is characterized by very small turbulent velocities (as represented by $u_*$) and poorly defined boundary layer heights. During the springs, turbulent energy is more closely tied to the mean tidal velocities, and the boundary layer height modulates with both the flood and ebb tides. In the next section we consider the mechanisms that determine this variability.

## 5. Conditions in the BBL

Based strictly on the depth-averaged tidal velocity (as in Fig. 6a), it is difficult to explain the variations evident in the friction velocity and the height of the BBL. In particular, there is a significant asymmetry between ebb and flood tide boundary layer parameters, even when the magnitude of the tidal velocity is equiva-

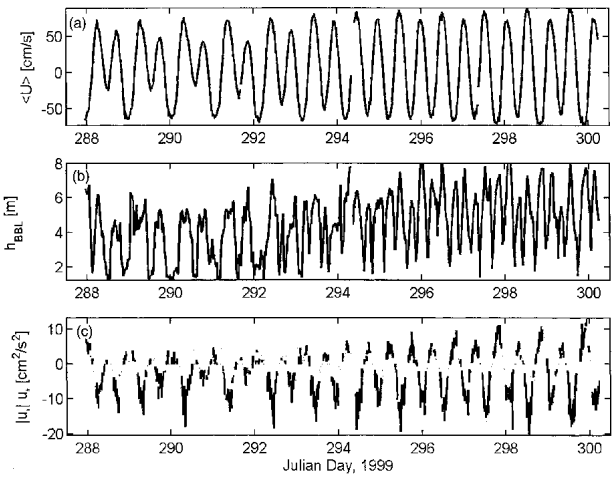


FIG. 6. Time variability of boundary layer characteristics: (a) depth-averaged mean velocity, (b) 1-h block averages of boundary layer height (requires three valid data points to include value here), and (c) signed friction velocity squared (sign based on sign of near-bed Reynolds stress).

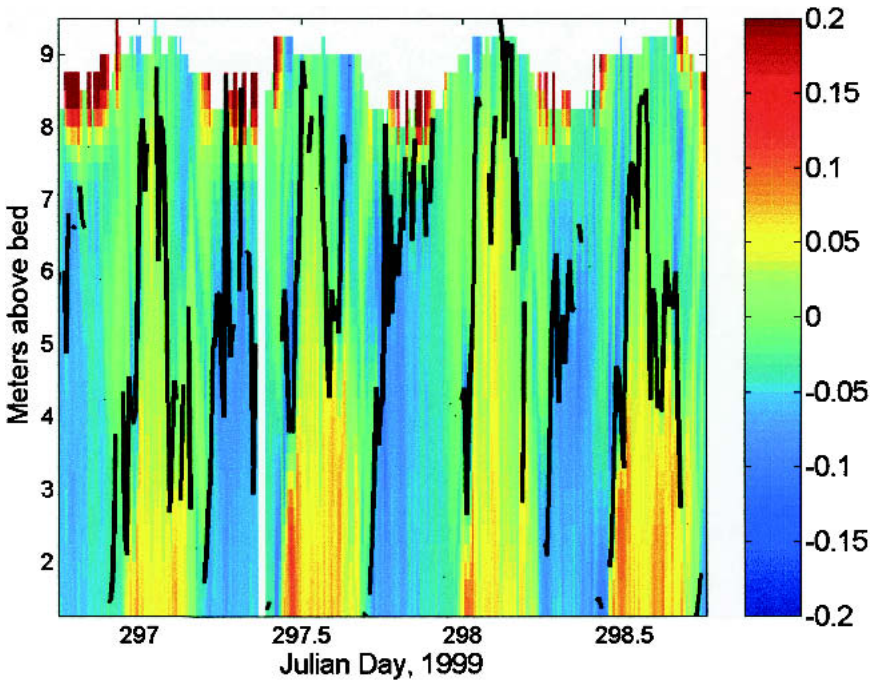


FIG. 7. Color contours of along-channel mean shear ($s^{-1}$) with boundary layer position overlaid. Positive values in the near-bed region are representative of flood tide, negatives are representative of ebb tide.

lent. In this section, we will compare the BBL parameters with other mean flow parameters from the same periods to establish the cause of the asymmetries evident in the friction velocity and BBL height.

### *a. Mean shear*

In Fig. 7, the vertical and temporal variability of the vertical shear of the along-channel mean velocity during the spring tides is overlaid with the height of the bottom boundary layer from the same period. During the ebb tides (negative shears), the height of the bottom boundary layer tends to coincide with a location of elevated midcolumn shear. This is particularly evident during the ebb tides at 297.25 and 297.75 (the large shears are characterized by the blue patches around 5–6 m above the bed). In contrast, the height of the BBL during flood tides coincides with a location of near-zero shear, or an extremum in the mean tidal velocity. It appears that during the ebb tides, the height of the BBL is being established by the interaction of shear and stratification at the top of the boundary layer. This is clearly not the case during the flood tide.

To examine the flood tide structure more clearly, Fig. 8 presents the mean velocity profiles, ensemble averaged based on the depth-averaged velocity. That is, all profiles during the two-week dataset with a depth-averaged velocity between 20 and 30 cm $s^{-1}$ were averaged together to produce one profile; this was repeated in 10 cm $s^{-1}$ intervals from $-100$ to 100 cm $s^{-1}$. Before examining the ebb–flood asymmetry a comment must be made about the near-surface reversal of the mean velocity. Throughout the two-week study, strong winds were relatively persistently blowing from west to east, creating a positive near-surface flow that either opposed the ebb tides or reinforced the flood tides.

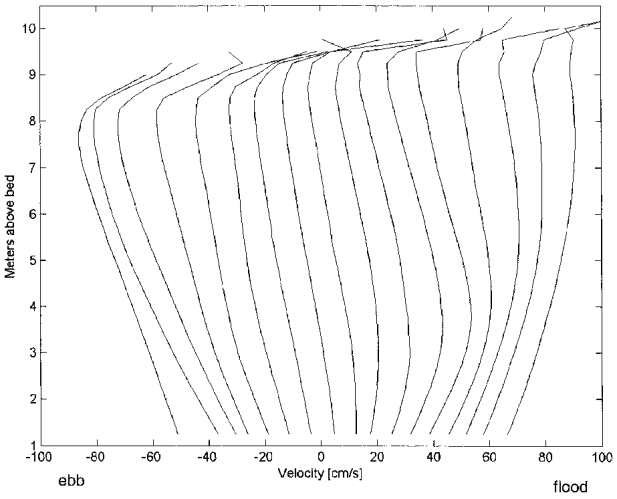


FIG. 8. Ensemble average profiles over entire dataset of mean velocity, with ensembles defined by 10 cm $s^{-1}$ bins of depth-averaged velocity. Profile in top 1–2 m is strongly influenced by wind stress, which was oriented from west to east (in the positive $x$ direction).

From the presentation in Fig. 8, it appears that this effect extended nearly a meter into the water column and appeared to have a velocity scale on the order of 20–30 cm $s^{-1}$. While this result is surely significant to the net transport in the system and the overall dynamics of the estuary, it is beyond the scope of this discussion of the bottom boundary layer.

Within the water column, the difference in the structure of the flows between ebbs and floods is clear in Fig. 8. On ebb tides, the velocity increases in magnitude away from the bed (until reaching the wind-influenced region near the surface). On flood tides, there is a clear subsurface maximum in the velocity that is about 3–4 m above the bed at low velocities but rises to a height of about 7–8 m at high velocities. This subsurface maximum is the location of zero shear and, from the results presented in Fig. 7, appears to represent the top of the bottom boundary layer.

To emphasize the asymmetry in the shear at the top of the BBL, we present histograms of the along-channel shear for vertical bins relative to $h_{\mathrm{BBL}}$ in Fig. 9. Within the BBL, the shear is negative on ebb tides (Fig. 9a) and positive on flood tides (Fig. 9d), as would be expected. At the top of the BBL, the ebb tide shear remains significantly negative (Fig. 9b). During the floods, however, the distribution of shear is centered around zero, with approximately equally likely positive and negative values (Fig. 9e). Above the BBL, while the ebb tide shear remains negative (Fig. 9c), the shear on the flood tide has reversed sign and is now negative (Fig. 9f). While there is obviously much spread in these distributions, it is clear that the structure of the shear in the water column is quite different between ebb and flood tides and that the top of the BBL on flood tides is tied to the location of zero shear, or maximum velocity.

### b. Stratification

During ebb tides, the presence of shear at the top of the BBL suggests that we should consider the interplay between shear and stratification at that location. To examine this interaction along with the height of the bottom boundary layer, we present (Fig. 10) the gradient Richardson number field overlaid with the boundary layer height for the same spring tide period considered in Fig. 7. While the Richardson number is a noisy parameter, because it is the ratio of two gradients, certain features are still evident in these data. In general, the bottom boundary layer is characterized by small values of $\mathrm{Ri}_g$, while the region above the BBL typically has larger values.

In fact, during the flood tides there are frequently regions with positive vertical density gradients (negative Richardson numbers), which are flagged here by the blocks of white in Fig. 10. These regions occur in the upper portions of the boundary layer (just below $h_{\mathrm{BBL}}$) at times 297, 297.5, and 298.05 and are convectively unstable, which helps to motivate the discussion of scaling the flood tide boundary-layer conditions in the next section.

On the ebb tides, the Richardson number is more moderate (approximately 0.1–0.25) and approaches

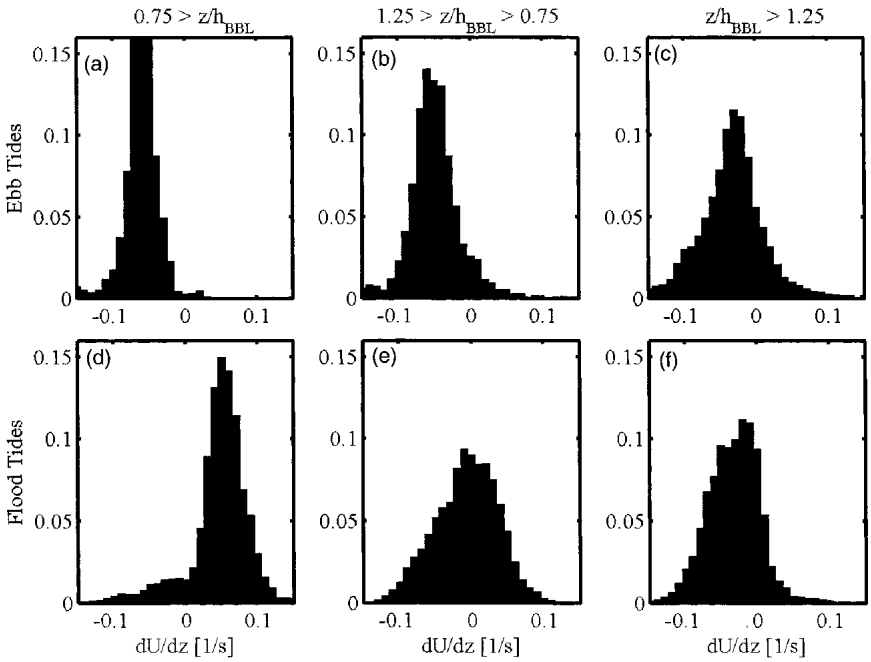


FIG. 9. Frequency distribution of vertical shear of along-channel flow as a function of tidal phase and position relative to the top of the boundary layer.

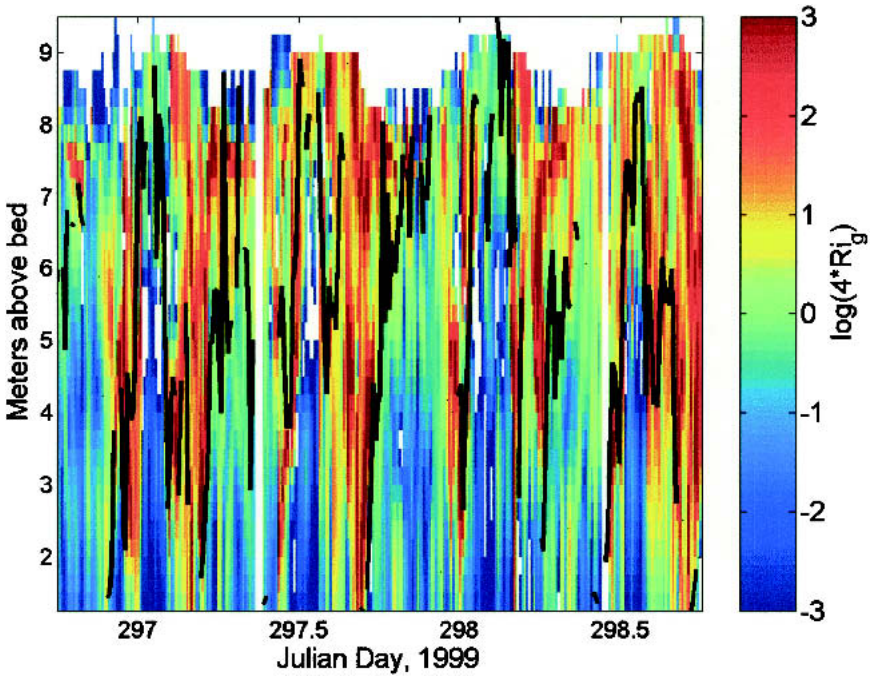


FIG. 10. Color contours of logarithm of gradient Richardson number (normalized by 1/4) with boundary layer position overlaid (black line). White blocks indicate regions with negative gradient Richardson number.

0.25 at the top of the BBL. To examine the vertical structure of the Richardson number more clearly, we present histograms of the gradient Richardson number binned by location relative to $h_{BBL}$. During the ebb tides $Ri_g$ transitions from values less than 0.25 within the BBL (Fig. 11a) to values larger than 0.25 above the BBL (Fig. 11c). The top of the boundary layer is marked by the transition through this value of $Ri_g$, as is evident in Fig. 11b.

During the flood tides, the variations of the gradient Richardson number are fundamentally different. Within the boundary layer is a broad range of values of $Ri_g$, including very small and, in fact, negative values (see Fig. 10 for the full range). At and above the boundary layer (Figs. 11e and 11f) Richardson numbers are large, which is expected based on the small values of the mean shear at these locations (Fig. 9).

### c. *Summary of BBL conditions*

The discussion of the previous sections has emphasized the conditions within the BBL and at the top of the BBL. The asymmetries between ebb and flood tides can now be summarized based on this discussion. During ebb tides, the boundary layer is characterized by mild stratification, and the top of the BBL is a location of relatively strong shear and stratification. It appears that the top of the BBL is characterized by gradient Richardson numbers around 0.25, which would suggest a balance between shear and stratification near that location (e.g., Turner 1973). During the flood tides, the boundary layer is unstratified and is frequently characterized by unstable density profiles. The top of the boundary layer is now the location of a minimum in the mean shear or a maximum of the mean tidal velocity.

This asymmetry between ebb and flood tides is most likely a result of tidal straining (Simpson et al. 1990). On ebb tides, the shear in the water column not only produces turbulence, but also provides a stabilizing buoyancy flux through the straining of the density field. On flood tides, the straining reverses and the mean shear produces a destabilizing buoyancy flux. At the point of maximum velocity, however, the sign of this buoyancy flux reverses, and above the maximum the straining of the density field is actually stabilizing. The height of the BBL on flood tides is therefore tied to the point at which the strain-induced buoyancy flux switches from destabilizing to stabilizing. On ebb tides, it appears that a competition between shear and strain-induced stratification defines the top of the BBL. In the next section, we examine a scaling approach to predicting the boundary layer height based on this discussion of the strain-induced buoyancy flux.

## 6. Scaling of boundary layer parameters

The discussion of the previous section suggests that the horizontal, advective buoyancy flux induced by straining of the density field (see, e.g., Simpson et al.

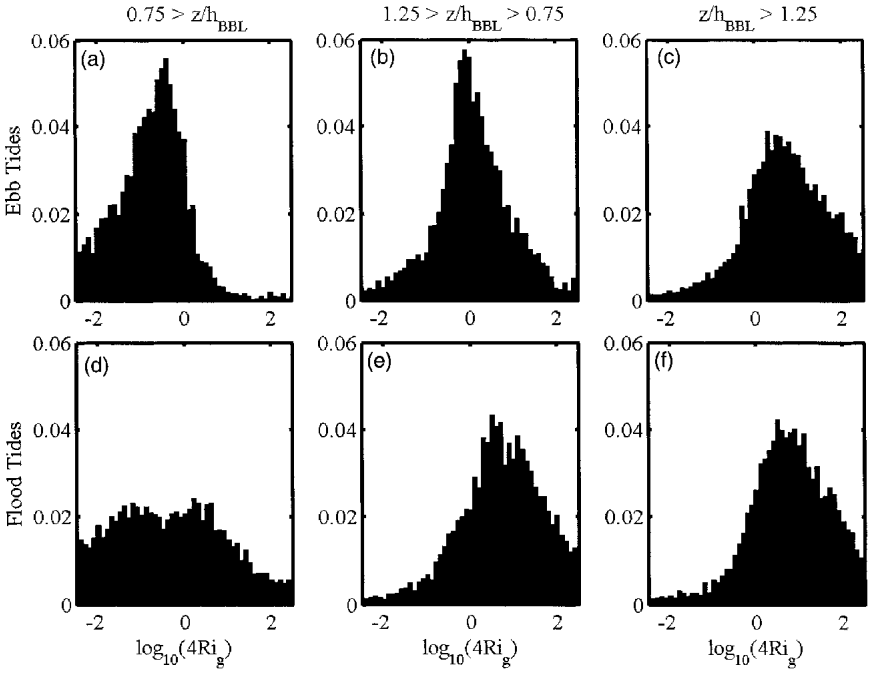


FIG. 11. Frequency distribution of gradient Richardson number as a function of tidal phase and position relative to the top of the boundary layer.

1990) is a critical factor in defining the boundary layer structure. To address this with a scaling approach, we need to define this strain-induced horizontal buoyancy flux, $B_h$, based on fundamental parameters of the flow. First, we assume that the density in the bottom boundary layer is uniform and is greater than the fluid overhead by an amount $\Delta\rho$ (Fig. 12). By analogy with the analysis of the surface mixed layer and a boundary buoyancy flux (see, e.g., Fischer et al. 1979), we use the change in density between the interior and the boundary layer ($\Delta\rho$) to define the buoyancy flux:

$$B_h = \frac{g}{\rho_0}\frac{\partial \Delta\rho}{\partial t} h_{\mathrm{BBL}}. \tag{2}$$

We now assume that the change in the density difference at $h_{\mathrm{BBL}}$ is driven by differential advection, or tidal straining. We therefore define

$$\frac{\partial \Delta\rho}{\partial t} = -\Delta U \frac{\partial \rho}{\partial x}, \tag{3}$$

where $\Delta U$ is the difference between the average velocity in the bottom boundary layer and the velocity just above the top of the boundary layer, and $\partial\rho/\partial x$ is the background longitudinal density gradient, which is assumed to be constant. This formulation assumes that the longitudinal tidal velocity dominates the straining of the density field. The role that the lateral circulation plays in the stratification dynamics is discussed by Lacy et al. (2003), and it appears that this component will be important to consider during the deceleration phase of the flood tide.

To define $\Delta U$, we integrate the expected velocity structure over the boundary layer, which results in

$$\Delta U = C\frac{u_*}{\kappa}, \tag{4}$$

where $\kappa$ is von Kármán's constant (0.41) and $C$ is a constant coefficient, which is 1 for the unstratified logarithmic layer. In a mildly stratified boundary layer (Turner 1973), the Monin–Obukhov profile, using the advective buoyancy flux to define an analogous length scale [see below, Eq. (8)], predicts a constant coefficient in Eq. (4) of 2. For the remainder of this discussion, however, we will assume $C = 1$ (note that $C = 2$ will simply result in a modified coefficient on the scaling

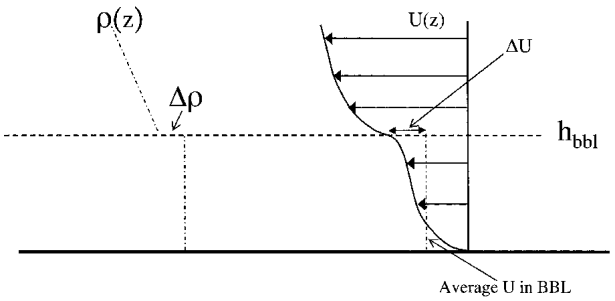


FIG. 12. Schematic of boundary layer assuming well-mixed density in the bottom boundary layer up to height $h_{\mathrm{BBL}}$.

results that follow), which then results in the following expression for the strain-induced buoyancy flux:

$$B_h = -\frac{g}{\rho_0}\frac{\partial \rho}{\partial x}\frac{u_*}{\kappa}h_{\mathrm{BBL}}. \tag{5}$$

Introducing a horizontal buoyancy frequency,

$$N_x^2 = -\frac{g}{\rho_0}\frac{\partial \rho}{\partial x},$$

this can be written more concisely as

$$B_h = \frac{u_*}{\kappa}N_x^2 h_{\mathrm{BBL}}. \tag{6}$$

In an unstratified boundary layer, we expect the shear production to decrease with height:

$$P = \frac{u_*^3}{\kappa z}. \tag{7}$$

The height at which the shear production is comparable to this horizontal buoyancy flux is analogous to the Monin–Obukhov length scale for a surface buoyancy flux (Monin and Obukhov 1954) and is defined as

$$L_h = \frac{u_*^3}{\kappa B_h} = \frac{u_*^2}{N_x^2 h_{\mathrm{BBL}}}. \tag{8}$$

The fact that this length scale depends on the height of the bottom boundary layer is a result of the fact that the buoyancy flux in this case is a distributed internal buoyancy flux, rather than the surface buoyancy flux in the case of surface heating or cooling. In the remainder of this section, we consider the turbulence energetics for ebb and flood tides.

### *a. Ebb tide scaling*

On the ebb tides, the strain-induced buoyancy flux is stabilizing and acts in opposition to the production of turbulent energy. The primary source of turbulence will be shear production, which must be sufficient to overcome the stratifying effects of the same shear through the straining term. In essence, we require that the vertical turbulent buoyancy flux be greater than the strain-induced buoyancy flux within the boundary layer in order to preserve well-mixed conditions. Outside the boundary layer, the turbulent buoyancy flux is insufficient to overcome the stratifying effects of the horizontal buoyancy flux. The top of the boundary layer is therefore the point at which these two buoyancy fluxes are in balance:

$$B_t = R_f P = B_h, \tag{9}$$

where $B_t$ is the (vertical) turbulent buoyancy flux and is modeled as a constant flux Richardson number ($R_f$) times the shear production $P$.

This condition defines a scaling for the boundary layer height through the dependence of $B_h$ on $h_{\mathrm{BBL}}$:

$$h_{\mathrm{BBL}} = R_f^{1/2}\frac{u_*}{N_x}, \tag{10}$$

a result that could have also been reached (to within the coefficient $R_f^{1/2}$) by setting $L_h = h_{\mathrm{BBL}}$ in the above definition of $L_h$ [Eq. (8)] and solving for $h_{\mathrm{BBL}}$. The fact that the boundary layer height scales with this length scale is not surprising, as $L_h$ represents the point at which shear production balances the stratifying horizontal buoyancy flux—which is precisely the condition imposed at the top of the boundary layer on ebb tides.

This expression for the boundary layer height relies on the independent evaluation of the second boundary layer parameter, $u_*$. Using a standard drag formulation for the friction velocity $u_*^2 = C_d U^2$, where $U$ is a reference mean velocity at the top of the boundary layer, we can rewrite Eq. (10) as

$$h_{\mathrm{BBL}} = H\left(\frac{R_f}{\mathrm{Ri}_x}\right)^{1/2}, \tag{11}$$

where $\mathrm{Ri}_x = N_x^2 H^2/(C_d U^2)$ is the horizontal Richardson number (Monismith et al. 1996; Stacey et al. 2001) and $H$ is the depth of the water column.

Before comparing these models with the estimates of $h_{\mathrm{BBL}}$ and $u_*$ based on the Reynolds stress data, we should note that during the ebb tides, the frequency of high-quality parameter fits was lower than on flood tides (Fig. 13). This is most likely due to the fact that the boundary layer tended to be thinner on ebb tides, particularly at low velocities, than on flood tides. As a result, we lose the ability to resolve this feature, and the quality of the parameter fit is reduced. Nonetheless, even at low tidal velocities, more than 25% of the profiles met our quality of fit criteria, and the scaling approach of Eq. (11) is compared with the data fits in Fig.

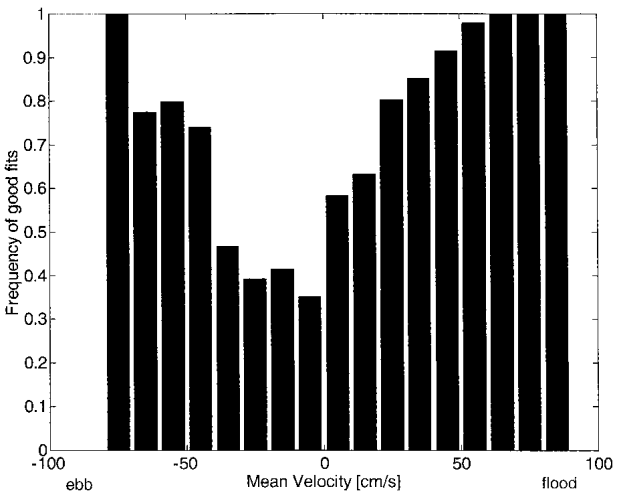


FIG. 13. Frequency of good fits to Reynolds stress profiles as a function of depth-averaged velocity (within 10 cm $s^{-1}$ bins).

14. The dashed lines in Fig. 14 indicate the mean value of each parameter resulting from bin-averaging based on the depth-averaged velocity, while the dotted lines illustrate the spread of the data. The models for the boundary layer parameters developed above [Eq. (11)] are represented by the solid line, where we have used $R_f = 0.2$ and an average of $N_x^2$ ($3.4 \times 10^{-6}$) over the entire dataset. The scaling prediction for boundary layer height, which is based on a shear–buoyancy balance, agrees very well with the observed values across all velocities. In Fig. 14b, the scale estimate of the friction velocity based on a constant drag coefficient and the boundary layer–averaged mean velocity is presented as a function of the depth-averaged velocity. The comparison between this scaling estimate and the observations is also encouraging, with the exception of a divergence between the scaling estimate and the actual value at low velocities. It appears likely that there is a vertical phase lag for the reversal of the tidal currents even in the lower couple of meters of the water column during the transition from ebb to flood tides. This phase lag means that the near-bed velocities have reversed into flood tide while the layer-averaged velocity is still near zero (and even ebbing), leading to an underestimate of the friction velocity. The fit of the scaling model to the remainder of the data (velocity of 20 cm $s^{-1}$ and greater) defines a drag coefficient of $C_d = 0.0017$, which is a significant reduction from the usually assumed value of 0.0025. The reduction in drag is most likely due to the effects of the straining of the density field, which reduces the vertical momentum transfer within the boundary layer, a topic that will be taken up again below in section 7.

### b. Flood tide scaling

On flood tides, the straining of the density field is destabilizing and is therefore a source of turbulent kinetic energy. In the limit of strong buoyancy forcing (i.e., free convection), we can assume that this convective source of energy is balanced by dissipation:

$$B_h = \frac{u_*}{\kappa} N_x^2 h_{\mathrm{BBL}} = \epsilon. \tag{12}$$

Using the scaling of Deardorff and Willis (1967), we can relate the convective velocity scale in the boundary layer to the dissipation rate as

$$u_t = (\epsilon h_{\mathrm{BBL}})^{1/3} = (B_h h_{\mathrm{BBL}})^{1/3}, \tag{13}$$

where we have applied the buoyancy–dissipation balance described in Eq. (12) and assumed that the bound-

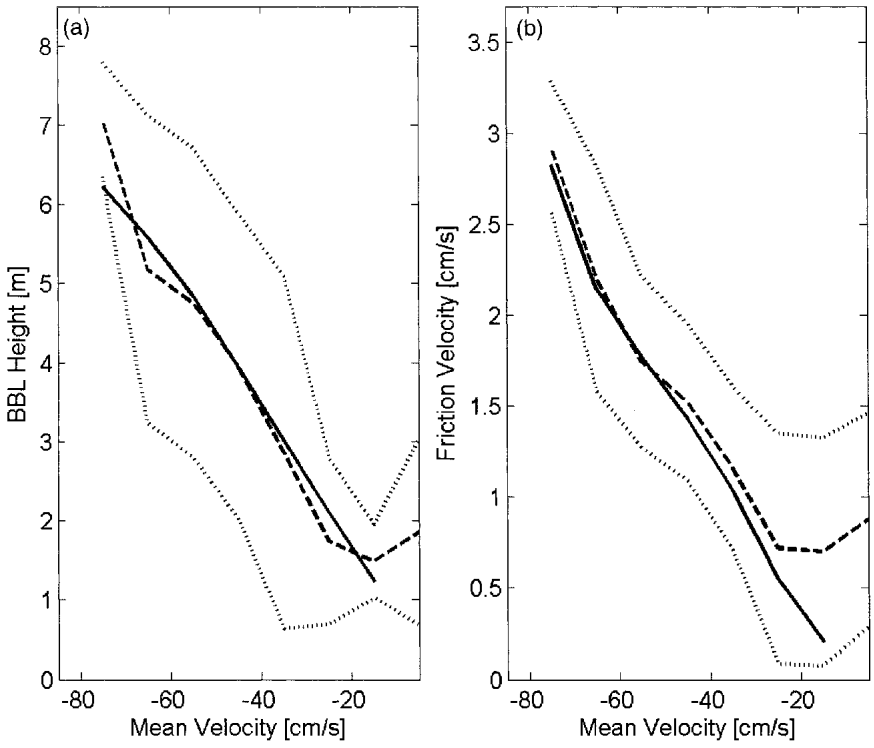


FIG. 14. Comparison between data and scaling estimates during ebb tides for (a) boundary layer height and (b) friction velocity. Dashed line is ensemble average of quantity from data (dotted lines ±1 std dev). Solid line in (a) is scaling estimate of boundary layer height, Eq. (11). Solid line in (b) is drag coefficient scaling, $u_*^2 = C_d U^2$, where $U$ is a boundary layer–averaged mean velocity and $C_d = 0.0017$. Note that each of the $x$ axes is the depth-averaged velocity.

ary layer height is the relevant length scale for the convective motions. Assuming that the convective velocities scale as the friction velocity, we can solve this equation for the friction velocity [using Eq. (6) for $B_h$]:

$$u_* = C(\Delta U N_x^2 h_{\mathrm{BBL}}^2)^{1/3}, \tag{14}$$

where $C$ is a coefficient of order 1 and $\Delta U$ represents the difference between the average velocity in the boundary layer and the flow velocity above the boundary layer (as discussed above).

Just as was the case on ebb tides, this model relies on an independent estimate of the second boundary layer parameter; in this case, $h_{\mathrm{BBL}}$. In the dataset under consideration here, the destabilizing buoyancy flux only extends up to the point of maximum velocity (Fig. 8). Above that point, the shear changes sign and the buoyancy flux becomes stabilizing. In the limit considered here, with buoyancy being a dominant source of turbulence in the bottom boundary layer, the boundary layer height should be related to this point where the sign of the buoyancy flux reverses. The height of this subsurface maximum appears to depend on lateral circulation and restratification of the channel under consideration (Lacy et al. 2003). A complete model of this dynamic would obscure the boundary layer scaling being presented here, so we simply assume that the location of the maximum tidal velocity, $Z_{\max}$ is a known parameter. With this definition, the scaling for the friction velocity is given by

$$u_* = C(\Delta U N_x^2 Z_{\max}^2)^{1/3}. \tag{15}$$

The flood tide boundary layer parameters are summarized in Fig. 15, in the same format as was used for the ebb tides in Fig. 14. The boundary layer height (Fig. 15a) is well predicted by the location of the velocity maximum, and both the data and the model indicate a near-constant boundary layer height at low velocities and a deepening of the boundary layer with increasing velocity above a transition point around 50–60 cm $s^{-1}$. With the exception of the lowest velocities, the friction velocity (Fig. 15b, solid line) is also well predicted by the convective scaling of Eq. (15), using $C = 1.4$. This scaling of the friction velocity assumes the limiting case where turbulent production is entirely dominated by buoyancy. The other limiting case would be that shear production is dominant, which would result in the same scaling presented for the ebb tide, namely, $u_*^2 = C_d U^2$. This scaling is also presented in Fig. 15b (dash–dot line,

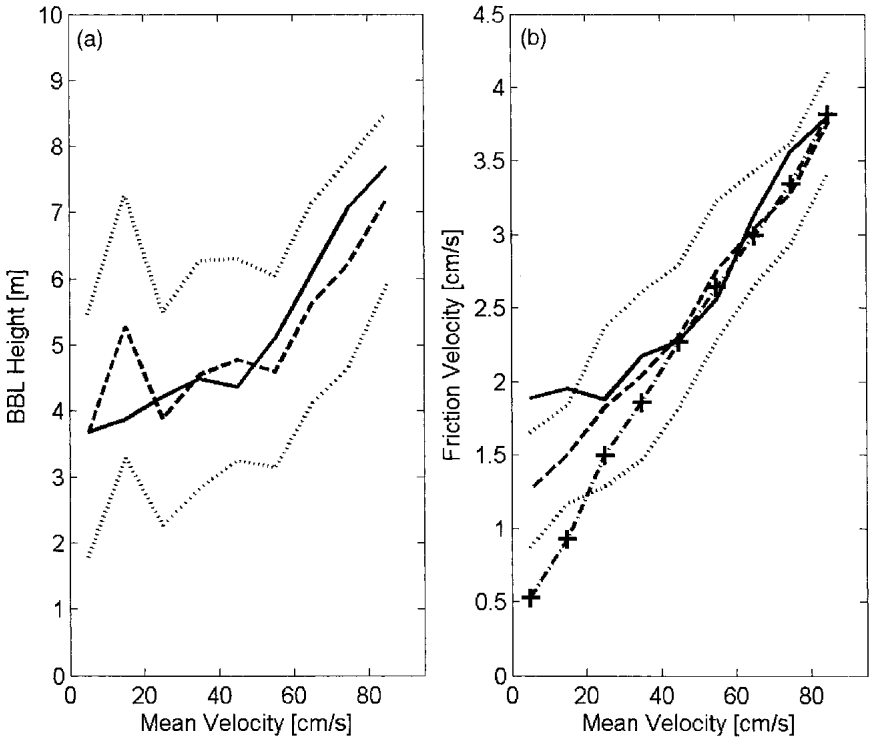


FIG. 15. Comparison between data and scaling estimates during flood tides for (a) boundary layer height and (b) friction velocity. Dashed line is ensemble average of quantity from data (dotted lines ± 1 std dev). Solid line in (a) indicates location of maximum of mean velocity. Solid line in (b) indicates the free convection scaling, Eq. (14); dash–dot line (with + overlaid) in (b) is drag coefficient scaling, $u_*^2 = C_d U^2$, where $U$ is a boundary layer–averaged mean velocity and $C_d = 0.0022$. Note that each of the $x$ axes is the depth-averaged velocity.

$C_d$ = 0.0022) and also agrees well with the observed values for tidal velocities greater than about 50 cm s$^{-1}$. It should be noted that other scalings are possible, such as that for forced convection (see, e.g., Turner 1973). However, any scaling for the friction velocity involving the tidal velocity, the horizontal density gradient and the boundary layer height will necessarily involve the tidal velocity and the boundary layer height in a way that their exponents sum to 1. Unfortunately, for tidal velocities greater than 50 cm s$^{-1}$, the boundary layer height increases linearly with tidal velocity so that the various scalings for the friction velocity will all have the same behavior in this domain. With the exception of the free convection scaling in Eq. (15), each of the alternative scalings tends to underpredict the friction velocity for tidal velocities less than 50 cm s$^{-1}$, and it appears that the convective scaling is most appropriate under these conditions. At higher velocities, the current dataset is not able to differentiate between the alternatives, but, as expected, the drag coefficient scaling does become more accurate at higher velocities.

## 7. Turbulence in bottom boundary layer

The relative importance of the straining of the density field, as estimated by the horizontal buoyancy flux $B_h$, can be evaluated by comparing this buoyancy flux with the shear production. The negative of the ratio of $B_h$ to $P$, which we will define to be the equivalent of a flux Richardson number (i.e., $R_{fh} = B_h/P$), with each quantity bin-averaged based on the depth-averaged tidal velocity, is presented in Fig. 16a, along with the boundary layer height estimated from the Reynolds stress data. Near the bed, shear production exceeds the buoyancy flux, and this ratio is small. On the ebb tides, the ratio becomes increasingly negative away from the bed, and the top of the boundary layer follows the contour where $B_h \approx -0.2P$, as was presented in the discussion of the ebb tide scaling for the boundary layer. On the flood tides, there is a similar structure, but with the ratio being positive around the top of the boundary layer, indicating the fact that the buoyancy flux is a source of energy.

A quantitative comparison of the average contribution to BBL turbulent energy is presented in Fig. 16b, where the average of $B_h$ and $P$ over the lower 75% of the BBL is presented. The ratio of these two quantities is presented in Fig. 16c, where we see that the buoyancy flux is equivalent to approximately 10% of the shear production during the peak tidal velocities on both ebbs and floods (a source during floods, a sink during ebbs). At smaller tidal velocities, however, the contribution to the turbulent energy budget is greater. During the ebbs, the buoyancy flux contribution approaches 25% of the shear production, consistent with the argument that the competition between the vertical and horizontal buoy-

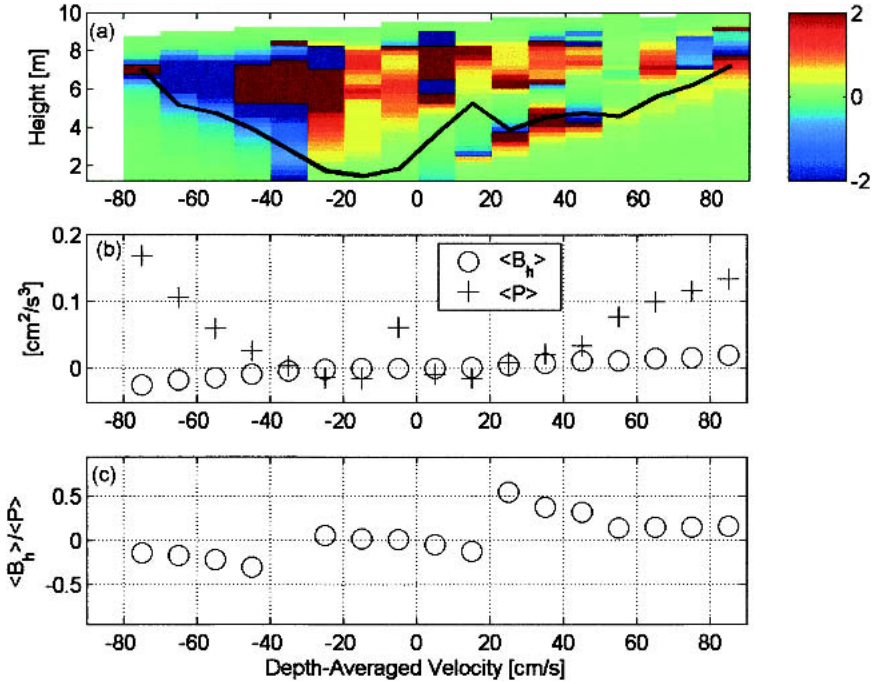


FIG. 16. Comparison of horizontal buoyancy flux and local shear production. (a) Ratio of $B_h$ to $P$ based on bin-averaged quantities (averaging based on depth-averaged velocity); solid black line shows boundary layer height based on same bin averaging. (b) Average values of $B_h$ (o) and $P$ (+) in lower 75% of BBL. (c) Ratio of values in (b), providing estimate of buoyancy flux contribution to the turbulent kinetic energy budget.

ancy fluxes defines the top of the boundary layer. During the floods, the contribution of the horizontal buoyancy flux to the production of turbulent energy is quite large, nearly 50% over the range of velocities from 20 to 50 cm $s^{-1}$. If this ratio exceeds ~5%, Turner (1973) suggests that a "free convection" scaling for the turbulent velocity scale [as presented in Eq. (15)] is the appropriate one, lending support to the scaling presented in Fig. 15b.

The fact that the horizontal buoyancy flux is an important contributor to the turbulent kinetic energy budget results in a significant asymmetry in turbulent kinetic energy between ebb and flood tides. The average turbulent kinetic energy in the bottom 75% of the BBL is presented as a function of depth-averaged velocity in Fig. 17a, where it is seen that the flood tide turbulent energy exceeds the energy on the ebb by as much as a factor of 2 for tidal velocities less than 65 cm $s^{-1}$. A direct comparison between flood and ebb turbulent energies is presented in Fig. 17b, and the TKE on flood tides is seen to exceed that on ebbs, except during the most energetic periods. To examine whether the reversing horizontal buoyancy flux can account for this asymmetry, we scale the TKE based on a local balance among dissipation, shear production, and the straining buoyancy flux. Scaling the dissipation rate as $\epsilon \approx q^3/l$ results in a dependence of the TKE on the shear production and the horizontal buoyancy flux to the two-thirds power. As a result, we have normalized the turbulent kinetic energy by

$$q^2_{\text{norm}} = q^2/(1 + R_{fh})^{2/3}, \tag{16}$$

where $R_{fh} = B_h/P$ and each quantity is an average over the bottom 75% of the BBL. The result of this normalization is presented in Fig. 17c, and it appears that the presence of the horizontal buoyancy flux quantified here predicts an ebb–flood asymmetry in the TKE that has a magnitude consistent with the observations.

Last, we examine the structure of the turbulence itself by defining the ratio of the vertical Reynolds stress and the turbulent kinetic energy:

$$S_m = \frac{|\overline{u'w'}|}{q^2}. \tag{17}$$

In many flows, the expectation for this quantity is 0.15 (Townsend 1976), but here we see (Figs. 18a,b) that the value of $S_m$ shifts between ebb and flood tides, with a reduction on ebbs and a slight increase on floods. The histograms presented in Figs. 18a and 18b summarize all the data, but to quantify this asymmetry, we note that the mean value of $S_m$ on ebb tides is 0.123 (median value of 0.125) and on flood tides is 0.157 (median value of 0.161). This variability cannot be explained by either the depth-averaged velocity (Fig. 18c) or the stratification and shear in the boundary layer (not shown) but is likely due to the fact that buoyancy is extracting energy from the vertical component of TKE on ebb tides, while on flood tides the convective motions associated with the destabilizing buoyancy flux produce motions more biased toward the vertical direction. The implication is that on ebb tides the turbulent energy is less effective at vertical momentum transfer than during the floods. This asymmetry is comparable in magnitude to the asymmetry in the energy itself and would compound the effects of the straining of the density field.

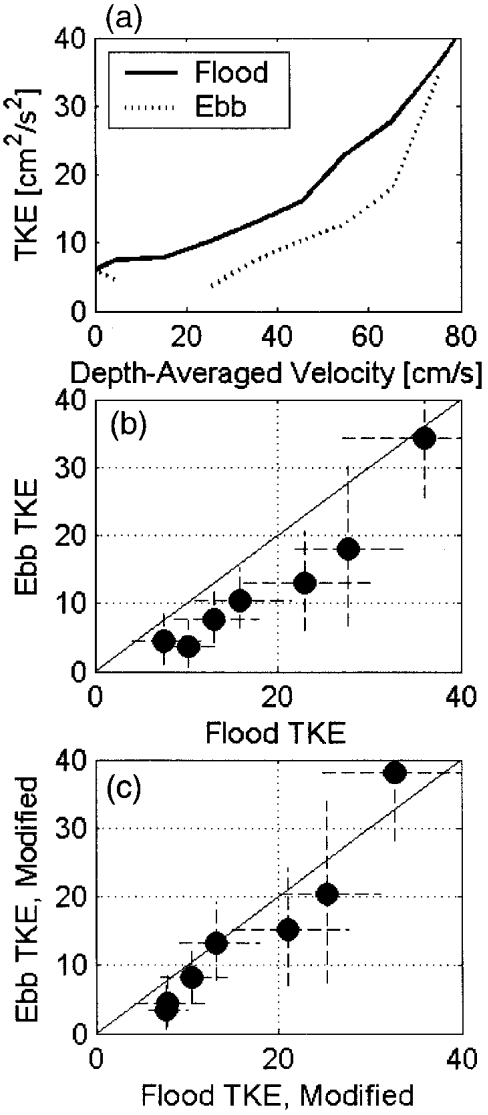


FIG. 17. Ebb–flood asymmetry in turbulent kinetic energy. (a) TKE as a function of depth-averaged velocity (bin-averaged values). (b) Comparison of flood and ebb TKE for equivalent depth-averaged velocities. (c) Comparison of flood and ebb TKE after normalizing by $(1 + R_{fh})^{2/3}$ to account for horizontal buoyancy flux (see text for details). In (b) and (c) dashed lines indicate range of 1 std dev.

## 8. Summary and conclusions

The tidal time-scale dynamics of the estuary dominate considerations of bottom boundary layer develop-

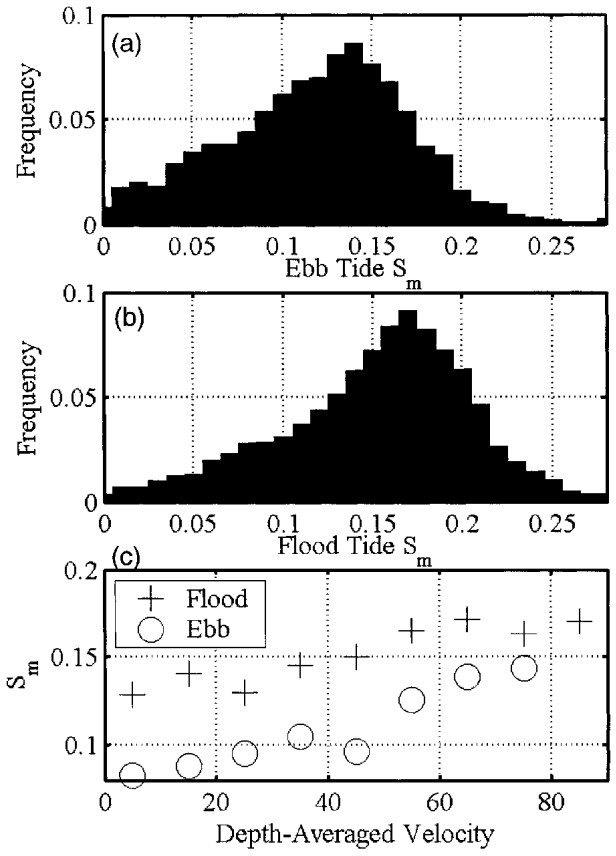


FIG. 18. Ebb–flood asymmetry in ratio of vertical Reynolds stress to TKE, $S_m$. (a) Histogram of $S_m$ on ebb tide: mean value = 0.123, and median value = 0.125; (b) histogram of $S_m$ on flood tide: mean value = 0.157, and median value = 0.161; and (c) comparison of bin-averaged values for $S_m$ on flood (+) and ebb (o) tides as a function of depth-averaged velocity: flood tide values exceed ebb tide values by as much as 50%.

ment, particularly the straining of the density field. On ebb tides, a stabilizing buoyancy flux is induced by differential advection along the density gradient. On flood tides, the buoyancy flux reverses sign and is destabilizing through much of the water column. This dynamic is analogous to the diurnal cycle in the lower atmosphere (Arya 1999) in which the boundary heat flux reverses from stabilizing to destabilizing between night and day.

An important difference between the two systems, however, lies in the fact that in the estuarine bottom boundary layer the buoyancy flux is distributed over the boundary layer by horizontal advection, as opposed to entering across the solid boundary. This distinction led to a modified form of the Monin–Obukhov scaling for the interaction of shear production and buoyancy flux. The reversal of the sign on the buoyancy flux between ebb and flood tides led to different turbulent energetics, with shear production being the primary source of turbulence on ebb tides and buoyancy forcing being an important contributor to production on floods. Using the Monin–Obukhov approach, scaling estimates of the boundary layer height and the friction velocity were found to agree quite well with the values observed in the estuary.

Within the bottom boundary layer, there is additional asymmetry created between ebb and flood tides due to the reversing sign on the buoyancy flux and its contribution to the turbulent kinetic energy. This leads to the turbulent energy on flood tides exceeding that on ebbs by as much as a factor of 2, even for equivalent tidal forcing. The vertical transfer of momentum by turbulence is further affected by a change in the ratio of the vertical Reynolds stress to turbulent kinetic energy. On ebbs, this ratio is reduced by about 25% relative to floods, which results in a severe reduction of momentum transfer on ebb tides versus floods.

Asymmetries in turbulent mixing can be an important contributor to residual circulation in the estuary (Geyer et al. 2000), and certainly to the salt balance. In order to effectively predict the details of this asymmetry, it is important to account for the horizontal buoyancy flux created by the straining of the density field by the tidal motions.

*Acknowledgments.* The data described here were collected as part of a collaborative research effort funded by the Office of Naval Research. The authors thank the U.S. Geological Survey and Stanford University, specifically Jon Burau, Jay Cuetara, Stephen Monismith, and Matthew Brennan, for their efforts during the data collection and their feedback during the preparation of the manuscript. Funding for the data analysis and manuscript preparation was provided by ONR (N00014-03-1-0617). The authors also thank two anonymous reviewers for their thorough feedback on the original manuscript.

## REFERENCES

Arya, S. P., 1999: *Air Pollution Meteorology and Dispersion*. Oxford University Press, 310 pp.

Burchard, H., O. Petersen, and T. P. Rippeth, 1998: Comparing the performance of the Mellor–Yamada and the $k$–$\epsilon$ two-equation turbulence models. *J. Geophys. Res.,* **103,** 10 543–10 554.

Cudaback, C. N., and D. A. Jay, 2000: Tidal asymmetry in an estuarine pycnocline. Part I: Depth and thickness. *J. Geophys. Res.,* **105,** 26 237–26 257.

Deardorff, J. W., and G. E. Willis, 1967: Investigation of turbulent thermal convection between horizontal plates. *J. Fluid Mech.,* **28,** 675–704.

DeBoor, C., 1978: *A Practical Guide to Splines.* Springer-Verlag, 392 pp.

Fischer, H. B., E. J. List, R. C. Y. Koh, J. Imberger, and N. H. Brooks, 1979: *Mixing in Inland and Coastal Waters*. Academic Press, 483 pp.

Geyer, W. R., J. H. Trowbridge, and M. M. Bowen, 2000: The dynamics of a partially mixed estuary. *J. Phys. Oceanogr.,* **30,** 2035–2048.

Gregg, M. C., 1987: Diapycnal mixing in the thermocline: A review. *J. Geophys. Res.,* **92,** 5249–5286.

Itsweire, E. C., J. R. Koseff, D. A. Briggs, and J. H. Ferziger, 1993: Turbulence in stratified shear flows: Implications for inter-

preting shear-induced mixing in the ocean. *J. Phys. Oceanogr.,* **23,** 1508–1522.

Jay, D. A., and J. D. Smith, 1990a: Residual circulation in shallow estuaries. Part 1: Highly stratified, narrow estuaries. *J. Geophys. Res.,* **95,** 711–731.

——, and ——, 1990b: Residual circulation in shallow estuaries. Part 2: Weakly stratified and partially mixed, narrow estuaries. *J. Geophys. Res.,* **95,** 733–748.

Lacy, J., M. T. Stacey, J. R. Burau, and S. G. Monismith, 2003: The interaction of lateral baroclinic forcing and turbulence in an estuary. *J. Geophys. Res.,* **108,** 3089, doi:10.1029/2002JC2001392.

Lu, Y. Y., and R. G. Lueck, 1999: Using a broadband ADCP in a tidal channel. Part II: Turbulence. *J. Atmos. Oceanic Technol.,* **16,** 1568–1579.

——, ——, and D. Y. Huang, 2000: Turbulence characteristics in a tidal channel. *J. Phys. Oceanogr.,* **30,** 855–867.

Monin, A. S., and A. M. Obukhov, 1954: Basic laws of turbulent mixing in the ground layer of the atmosphere. *Acad. Sci. USSR Leningr. Geophys. Inst.,* **24,** 163–187.

Monismith, S. G., J. R. Burau, and M. T. Stacey, 1996: Stratification dynamics and gravitational circulation in northern San Francisco Bay. *San Francisco Bay: The Ecosystem,* T. Hollibaugh, Ed., Pacific Division of the American Association for the Advancement of Science, 1–31.

Peters, H., and R. Bokhorst, 2000: Microstructure observations of turbulent mixing in a partially mixed estuary. Part I: Dissipation rate. *J. Phys. Oceanogr.,* **30,** 1232–1244.

——, and ——, 2001: Microstructure observations of turbulent mixing in a partially mixed estuary. Part II: Salt flux and stress. *J. Phys. Oceanogr.,* **31,** 1105–1119.

Rippeth, T. P., N. R. Fisher, and J. H. Simpson, 2001: The cycle of turbulent dissipation in the presence of tidal straining. *J. Phys. Oceanogr.,* **31,** 2458–2471.

——, E. Williams, and J. H. Simpson, 2002: Reynolds stress and turbulent energy production in a tidal channel. *J. Phys. Oceanogr.,* **32,** 1242–1251.

Simpson, J. H., J. Brown, J. Matthews, and G. Allen, 1990: Tidal straining, density currents, and stirring in the control of estuarine stratification. *Estuaries,* **13,** 125–132.

Stacey, M. T., 1996: Turbulent mixing and residual circulation in a partially stratified estuary. Ph.D. thesis, Stanford University, 209 pp.

——, S. G. Monismith, and J. R. Burau, 1999a: Observations of turbulence in a partially stratified estuary. *J. Phys. Oceanogr.,* **29,** 1950–1970.

——, ——, and ——, 1999b: Measurements of Reynolds stress profiles in unstratified tidal flow. *J. Geophys. Res.,* **104,** 10 933–10 949.

——, J. R. Burau, and S. G. Monismith, 2001: Creation of residual flows in a partially stratified estuary. *J. Geophys. Res.,* **106,** 17 013–17 037.

Townsend, A. A., 1976: *The Structure of Turbulent Shear Flow*. Cambridge University Press, 429 pp.

Trowbridge, J. H., and S. J. Lentz, 1991: Asymmetric behavior of an oceanic boundary layer above a sloping bottom. *J. Phys. Oceanogr.,* **21,** 1171–1185.

Turner, J. S., 1973: *Buoyancy Effects in Fluids*. Cambridge University Press, 367 pp.